Shock-wave-induced optical emission from sapphire in the stress range 12 to 45 GPa: Images and spectra

D. E. Hare and N. C. Holmes

University of California, Lawrence Livermore National Laboratory, Livermore, California 94550

D. J. Webb

University of California, Davis, Davis, California 95616

We took short-duration exposure images and spectra of the optical emission from shock-compressed single-crystal sapphire (α-Al$_2$O$_3$) for three common crystal orientations: *c*-plane {0001}, *a*-plane {11$\bar{2}$0}, and *r*-plane {1$\bar{1}$02}. The images show that this emission is not homogeneous, but is spatially localized. For a given shock stress, the *r*-plane orientation consistently produces less emission intensity than the other two orientations. The emission spectra were fit to a gray-body function. Apparent temperatures range between 4700 and 5400 K, consistent with earlier spectroscopic work. The value of the apparent emissivity in the spectral fits is very low, between 2×10^{-3} and 6×10^{-3}. We attribute the emission source to be shear banding which is not associated with twinning or slip on {0001}.

PACS number(s): 62.50.+p

I. INTRODUCTION

A shock wave is a large-amplitude compressive stress wave which is characterized by a very abrupt region of transition from the uncompressed state to the compressed state (the "shock front").[1] Shock waves are related to sound (small-amplitude stress wave phenomena) and a weak shock wave propagates through a solid material at a speed comparable to the longitudinal sound speed in that same material. However, shock wave propagation speed increases steadily with increasing amplitude and a strong shock wave will propagate somewhat faster than the sound speed.

A one-dimensional steady shock wave, such as can be launched by the high velocity co-planar impact of a flat projectile with a flat target, is a very convenient way of generating large compressive stresses (readily in excess of one million atmospheres for many solid materials). Compression using a strong shock wave has been an important technique for attaining high pressures in condensed matter for many years.[2] Optical experiments on shock compressed samples frequently require the use of an optical window. Such a window has two main functions: to allow optical radiation access to the sample surface and to pressurize the sample surface. For example, a window is useful for studying an opaque material such as a metal. For metals, all optical measurements are restricted to within a few nanometers of the surface. However, a free surface is not useful for observing high-pressure states because a free surface cannot be pressurized, hence the need for a transparent window.

Not all transparent, rigid materials make suitable windows for this application. A popular material for many shock-compression applications is lithium fluoride (LiF).[3] The outstanding feature of LiF is its optical transparency under shock load conditions. Its shortcoming is that it has a relatively low shock impedance ($\equiv$ mass density $\times$ shock velocity), making it rather inefficient at pressurizing samples. Sapphire, on the other hand, would seem to have

superior window qualities. It has a rather high shock impedance among window materials. Sapphire is readily synthesized in large, pure, single-crystal windows of high structural perfection and is relatively inexpensive. The room-temperature and pressure (RTP) transparency of the material is quite good. The useful transparency range of as-grown synthetic material extends from 250 to 4500 nm, and this range can be extended in the ultraviolet to 140 nm with special processing.[4]

Unfortunately, this excellent transparency under RTP conditions deteriorates significantly under shock loading conditions. Very early in the history of the velocity interferometer system for any reflector (VISAR) (Ref. 5) measurements it was discovered that sapphire was unsuitable as a VISAR window when its Hugoniot elastic limit (HEL) is exceeded. (The HEL is the maximum shock stress that a sample will sustain without undergoing plastic deformation. It generally depends on crystal orientation for single-crystal samples.) Urtiew investigated the suitability of sapphire as a pyrometry window for 900 nm light.[6] He concluded that under these conditions sapphire was transparent at 85 GPa but showed loss of transparency above 100 GPa. His crystal orientation was given as 60° off of the *c*-axis. Regarding the work of Urtiew, McQueen and Isaak pointed out that the apparent loss of transparency could have been caused by the reference window material (sodium chloride) becoming hot and optically thick.[7] McQueen and Isaak interpreted their own results as indicating that sapphire was probably transparent up to 200 GPa. Webb, using light of wavelength 300–500 nm, demonstrated that for the *c*-plane ("Z-cut") orientation, loss of transmission began at the *c*-plane HEL and increased dramatically with additional increase in stress.[8] He was unable to distinguish between scattering and absorption as the mechanism responsible for loss of transmission. No wavelength dependence was found for this transmission loss between 300 and 500 nm. Kondo found that the emission spectra of shock-compressed sapphire between 15.6 and 84.7 GPa could be described as gray-body radiation with a fitting

temperature of about 4930 K$\pm$470 K.[9] Within the uncertainty in his data, this fitting temperature appeared to be independent of shock stress, but that the fitting emissivity of his results did increase with shock stress. Kondo's fitting temperature is much higher than the 310–620 K computed for sapphire in the same shock-stress range[10] based on its thermodynamic properties and the conservation equations of fluid dynamics as specifically modified for shock compression.[11] Kondo attributed the emission mechanism in sapphire to "triboluminescence with a long decay time." Extending Webb's afore-mentioned work, Kwiatkowski and Gupta studied the emission, extinction (450–650 nm), and scattering (514.5 nm) of c-plane sapphire above the HEL.[12] They found weak, broadband emission (which was, however, too narrow to be gray body), extinction which was more effective for shorter wavelengths, and showed that at least part of that extinction was due to scattering. By further assuming that all extinction was due to scattering, they found the extinction was consistent with a distribution of Mie scatterers small compared to a wavelength of light.

Regarding the imaging of shock-induced emission in other transparent crystals, Brooks demonstrated that the crystal orientation of α-quartz made a striking difference in the appearance of the emission images.[13] He concluded that the emission for the X orientation was associated with piezoelectric activity, whereas emission from the Y and Z crystal orientations was a more common type of triboluminescence and was similar to shock-induced emission seen in fused silica. (Note: The piezoelectric effect is symmetry forbidden in sapphire.) Brannon, Morris, Konrad, and Asay showed images and optical pyrometry measurements of X-cut α-quartz and another transparent and piezoelectrically active crystal, Z-cut lithium niobate.[14] The quartz images revealed intense, spatially localized emission coming from distinct crystallographic planes, which the authors identified as known fracture planes in quartz. They showed that the onset of emission occurred at dynamic yielding and that it eventually became spatially homogeneous as stress increased. They found the emission from quartz to be bandlike and similar to photoluminescence spectra from structural defects of quartz.

The intent of this work is to study shock-compression-induced optical emission in fully oriented single-crystal sapphire by concurrent spectroscopic and imaging measurements, specifically to improve understanding of the connection between sapphire crystallography and this emission. More generally we seek to further understand optical windows, including their deformation mechanisms, and eventual failure as an effective optical window under shock-compression conditions.

The present work extends previous work by concurrently examining the spatial and spectral distribution of shock-induced emission in sapphire. It shows how this emission is affected by crystal orientation and shock stress.

II. EXPERIMENTAL PROCEDURE

Colorless, synthetic, single-crystal α-Al$_2$O$_3$ (sapphire) was purchased as disks 3.00 mm thick by 15.0 mm diameter with the disk surface in the basal or c-plane {0001}, a-plane
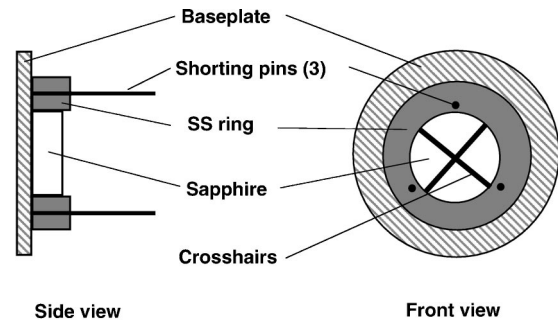

FIG. 1. Front and side view of sapphire targets. The baseplate is made of either 304 stainless steel or iron. The sapphire sample has a 500-nm-thick chromium coating which faces the baseplate (not shown). The coated side of the sapphire is bonded to the baseplate with a very thin layer of epoxy. "SS" stands for stainless steel.

{11$\bar{2}$0}, and r-plane {1$\bar{1}$02} orientations from Meller Optics, Inc. (see Appendix B). Sample purity was 99.99% or better. Some of the r-plane, and all of the c-plane and a-plane samples were fully oriented by Laue backscattering.[15] The remainder of the r-plane samples were fully oriented using crossed polarizers (i.e., location of the optic axis). The fully oriented samples were indexed with the appropriate markings so that full sample orientation could be reconstructed in the emission images.

The sample construction is outlined in Fig. 1. The diameter of a sample was fitted into a stainless steel ring to minimize potential emission due to lateral unloading of the sample. The ring was blackened to minimize spurious optical reflection. The ring-sample assembly was bonded to a baseplate of either 1.8-mm-thick stainless steel or 2.0-mm-thick iron using a thin layer of epoxy. The sample surface bonded to the baseplate had been coated with 500 nm of chromium so that the baseplate-epoxy-sample joint (a potential source of spurious emission) was hidden from imaging and spectral view. Electrical shorting pins were used to trigger the diagnostics and to determine impactor tilt.

Shock compression was achieved by impacting the sample with a 1.6-mm-thick tantalum impactor plate, mounted in a polycarbonate sabot, which was launched from a two-stage light gas gun.[16] For impactor velocities below 1000 m/s a single-stage gas breech gun was used. The projectile impacts the sample assembly from the baseplate side, launching a shock-compression wave which propagates toward the sample. The direction of propagation of the shock wave is normal to the specified orientation plane. For example, a shock-compressed r-plane sample means that a shock wave was launched in single-crystal sapphire with direction of propagation normal to {1$\bar{1}$02} (and consequently the wave front was co-planar with {1$\bar{1}$02}). The experimental apparatus is illustrated in Fig. 2.

Shock stresses in sapphire were computed according to the proceedure outlined in Appendix A using measured impactor velocities and the known mass densities and Hugoniot data of the baseplate, sapphire,[17] and impactor materials.[18] Elastic wave data for computing elastic stresses in c-plane sapphire were taken from Graham and Brooks.[19] There are two special issues to be addressed concerning our reported
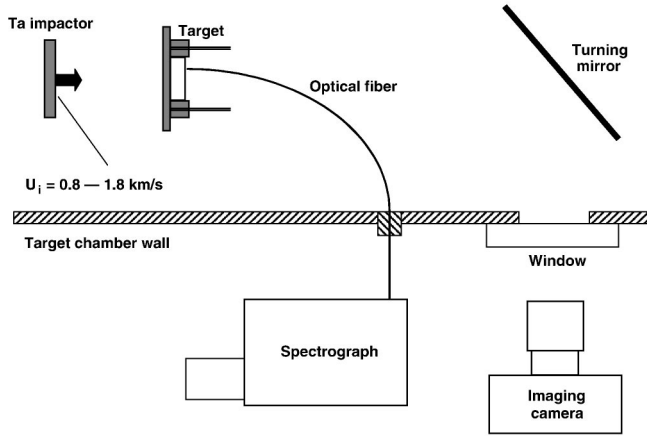
FIG. 2. Schematic of experimental setup. Both imaging camera and spectrograph have associated controllers, pulsers, and data acquisition computers (not shown).

values of shock stress. First: Shock-stress for each crystal orientation theoretically should be evaluated using Hugoniot data for the same orientation. Second: There are large uncertainties in the value of shock stress near the HEL, as with the value of the HEL itself.

Regarding the first issue, for the elastic case we used only c-plane Hugoniot data to evaluate stress in c-plane samples, so this issue does not arise for our elastic stresses. For the plastic Hugoniot we used the Los Alamos compiled data[17] for sapphire of unspecified orientation and applied it to all three of our crystal orientations. Based on recent sound speed work[20] for a-, c-, and r-plane sapphire, we believe the worst-case scenario is a 4% error in shock stress for our target geometry due to this particular issue.

Regarding the second issue, as mentioned previously, we used the Los Alamos compiled plastic Hugoniot data for presumed plastic stresses above 13 GPa whether it was appropriate or not. In fact, the data composing this Hugoniot extends from a nominal 21.3 to 143.5 GPa. Plastic stresses reported between 13 and about 30 GPa should be considered very approximate, as well as elastic stresses above 12 GPa. In anticipation that there may be a future resolution to this problem which could result in more accurate evaluation of sapphire shock stress in this troublesome range, Table I reports the necessary data to re-evaluate this quantity.

Light for spectral analysis was collected by a 0.22 numerical aperture 200-micron-silica-core optical fiber which was mounted against the free surface of the sample. This fiber led out of the target chamber to a single monochromator fitted with a gated, intensified diode array detector. The spectrograph acquired one exposure per experiment. Exposure length ranged from 50 to 140 ns but the spectral exposure gate pulse was centered on the time when the shock wave was halfway through the sapphire sample. The range of wavelengths collected was 280–730 nm and the spectrograph was operated with a resolution of 15 nm. A quartz-halogen illuminator was calibrated as a portable secondary standard of spectral irradiance, and used to calibrate the

TABLE I. Data for recomputing shock stresses in sapphire: "iron" is pure iron. "SS" is 304 stainless steel. "incident stress" is the shock stress in the baseplate created by the impactor-baseplate impact and is incident on the baseplate-sapphire junction. "Sample" gives the crystal orientation of the sapphire. "Nominal stress" is the approximate stress of transmitted shock wave in sapphire. Stresses computed using the elastic sapphire Hugoniot are in parentheses.

Shot number	Baseplate	Incident stress (GPa)	Sample	Nominal stress (GPa)
627	iron	20.27	r	20.4
628	SS	22.77	c	21.1
630	SS	23.42	a	21.7
631	SS	53.56	r	47.2
635	SS	50.51	c	44.7
636	SS	50.23	a	44.5
637	SS	46.83	r	41.6
638	SS	45.14	c	40.2
822	SS	22.96	c	21.2
823	SS	14.00	c	13.2 (15.0)
824	SS	10.61	c	10.1 (11.5)
825	SS	23.60	c	21.8

spectrograph for spectral irradiance at the entrance side of the optical fiber.

The sample emission for the image was relayed by a mirror through a target-chamber window to the imaging camera. The imaging camera was fitted with an f/2.8, 180 mm camera lens for good filling of the intensified CCD camera (ICCD) array by the image. One image was acquired per experiment and the exposure duration varied between 12 and 50 ns. Typically the imaging exposure gate pulse was centered at the time where the shock wave was computed to be about one-third to halfway into the sample. The imaging camera was operated without bandpass filters and was sensitive to wavelengths in the approximate range of 350–850 nm.

III. RESULTS

Many of the lower stress experiments did not generate enough signal for a spectrum. However, when spectra were successfully acquired they were flat and featureless, with spectral irradiance being fairly evenly distributed at all wavelengths within the spectrograph range. In Fig. 3 we show a raw sample spectrum (shot 635, c-plane 45 GPa) along with the secondary standard (illuminator), and a dark count, with the sample and standard spectra offset vertically for illustrative clarity. In the sample spectrum chosen for this figure, there appears to be just a hint of a low, very broad feature which appears as though it were centered at roughly 730 nm, but this feature was not reproducible. All experiments which yielded a usable emission spectrum (i.e., measurably different from a dark spectrum) were qualitatively similar to that of Fig. 3 including two spectra at the lower end (20–22 GPa) of the stress range studied.

We used a standard of spectral irradiance to calibrate our spectrograph prior to each experiment. The spectrograph was always calibrated such that a known spectral irradiance when
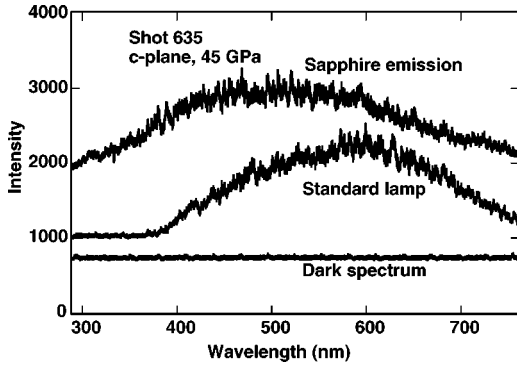
FIG. 3. Examples of raw spectra: (i) Shock-induced emission spectrum from shot 635 (*c*-plane at 45 GPa, offset by 1000 counts). (ii) portable standard of spectral irradiance, offset by 300 counts. (iii) dark count spectrum.

applied to the entrance end of the optical fiber (the end which would be eventually butted up against the sample) gave a certain measured response of the spectrograph. This allows us to reconstruct from our spectra that component of average spectral irradiance at the fiber entrance position which was propagated by the fiber (i.e., within its numerical aperture). We then did a gray-body fit to this emission, with apparent emissivity ϵ' and apparent temperature T' being the fit parameters (also see Appendix C):[21,22]

$$W'_\lambda = \frac{\epsilon' 2\pi hc^2}{\lambda^5 \left(\exp\left(\dfrac{hc}{\lambda kT'} \right) - 1 \right)}. \tag{1}$$

Here W'_λ is that portion of the average spectral irradiance at the fiber entrance which is within the acceptance cone of the fiber, h is the Planck constant, c is the speed of light in vacuum, k is the Boltzmann constant, λ is the wavelength of the radiation (in air). We applied this fit to all experiments which gave usable emission spectra. We mention here that the fit to a gray body is an expedient: we reserve judgment as to whether this light is or is not thermal incandescence. Figure 4 shows two representative examples: shots 635 (*c*-plane 45 GPa) and 636 (*a*-plane 45 GPa). The former yielded 4780 K ($\pm 3\%$) with an ϵ' of 2.0×10^{-3} ($\pm 17\%$). The latter yielded 5383 K ($\pm 7\%$) with an ϵ' of 5.4×10^{-3} ($\pm 32\%$). These temperature and emissivity uncertainties are generated by the fitting routine and are only indicative of the goodness of fit of the gray-body function to the data. The fits are marginal, but the conclusion is in good quantitative agreement with Kondo regarding T'. Our ϵ' also compare favorably to emissivity values plotted in Kondo's Fig. 5, which appear to center at about 5×10^{-3} at about 45 GPa.

Figure 4 also shows an attempted blackbody fit of the same data sets (i.e., ϵ' was constrained to be 1). Clearly, these two blackbody fits are not right at all, but this attempted procedure illustrates two interesting points: (i) T' of a gray-body fit is derived from the shape of the spectrum. Because the measured spectral irradiance is quite flat across the range 400–750 nm the T' are coming in around 5000 K, which is peaked near the middle of this wavelength range.
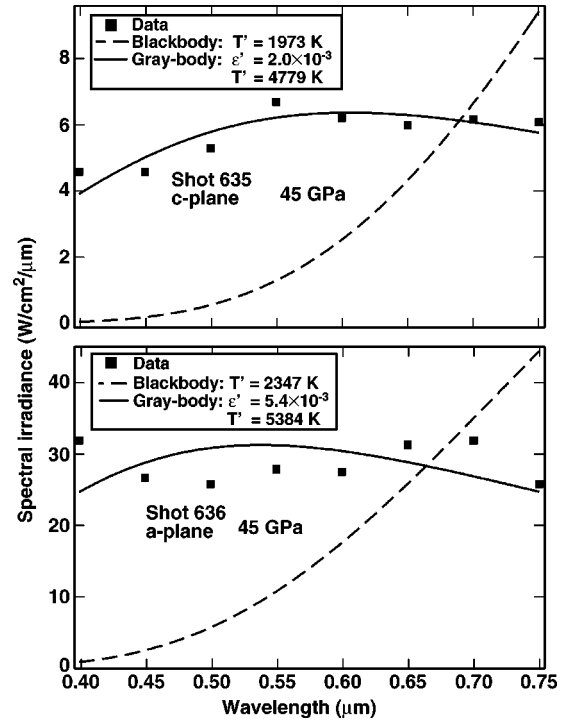

FIG. 4. A gray-body and blackbody fit of the spectra of shock-induced emission from sapphire for (a) *c*-plane at 45 GPa, and (b) *a*-plane at 45 GPa.

(ii) ϵ' simply scales the gray-body function without changing its shape. Thus the T' are around 5000 K because the shape of the emission spectra are almost flat over the observed range of wavelengths. ϵ' is very low because the spectral irradiance of the emission measured at the entrance of the optical fiber is very low compared to the spectral radiant emittance of a 5000-K blackbody surface.

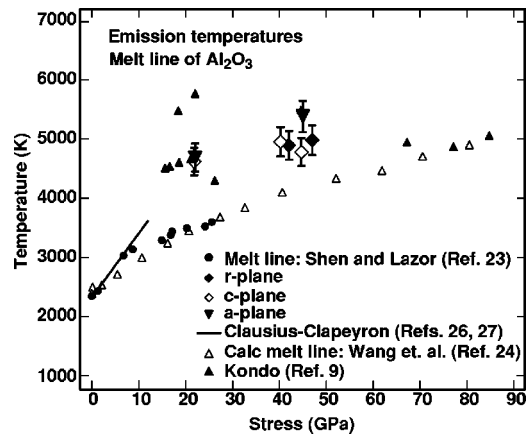Plotted in Fig. 5 are the T' for all our successfully ac-

FIG. 5. Measured gray-body T' for shock-induced emission from sapphire versus shock stress, plotted with sapphire melt line versus hydrostatic pressure. Measured gray-body shock T' are from this work and Kondo. Measured melt-line data are from Shen and Lazor. Calculated melt line data are from Wang, Mao, and Saxena. The Clausius-Clapeyron melt line slope, evaluated from atmospheric-pressure data, is also shown.
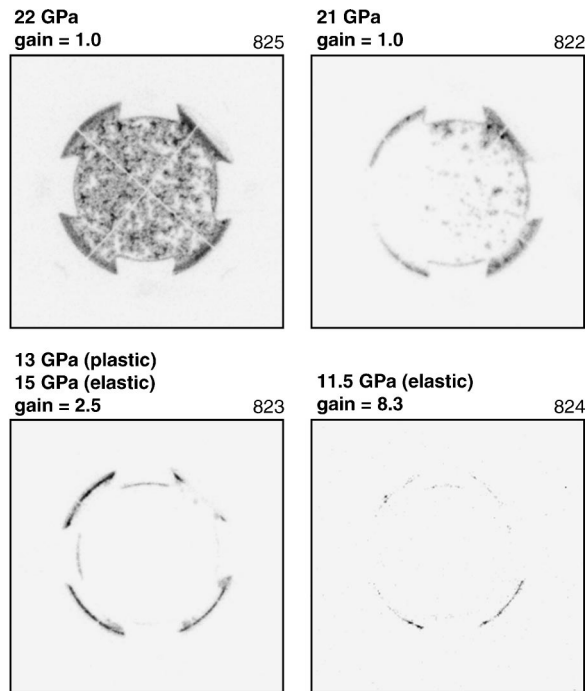
22 GPa
gain = 1.0   825

21 GPa
gain = 1.0   822

13 GPa (plastic)
15 GPa (elastic)
gain = 2.5   823

11.5 GPa (elastic)
gain = 8.3   824

FIG. 6. Shock-induced emission (negative) images of c-plane sapphire at shock stresses between 11.5 and 22 GPa. Relative camera gain is also given. Greater gain means increased sensitivity to emission. Thus the real disparity in emission intensity is even greater than is apparent, because the lower the stress, the higher the sensitivity the camera was operated at. (a) 22 GPa, gain=1. (b) 21 GPa, gain=1. (c) 13 GPa (assuming plastic Hugoniot) or 15 GPa (assuming elastic), gain=2.5. (d) 11.5 GPa (elastic), gain=8.3.

quired spectra together with the gray-body fit data of Kondo. Our T' are the same to within the error bars and are in very good agreement with his results. Kondo measured this property over a larger shock stress range (15.6–84.7 GPa) for sapphire of unspecified crystal orientation. He found that his T' were independent of shock stress. Our data augment Kondo's original result by showing that T' does not seem to depend on crystal orientation. Also shown in Fig. 5 are melting temperature data from Shen and Lazor[23] and computed melting temperatures from Wang, Mao, and Saxena.[24] The Clausius-Clapeyron relation[25] was evaluated using one atmosphere melting point data from various sources[26,27] and therefore the result should accurately represent the slope of the melting curve for low pressures. For shock emission T' the stress variable of Fig. 5 is shock stress (i.e., the normal stress on a plane which is both behind, and co-planar with, the wave front). For melting curve results, it is hydrostatic pressure. For an inviscid fluid there is no difference between shock stress and pressure, but for materials of finite strength the final strain state achieved by a shock wave and a hydrostatic compression are distinctly different. In the extreme case of an isotropic elastic medium, a stress wave results in uniaxial strain whereas hydrostatic compression results in isotropic strain. Our point here is that melting temperature versus shock stress will not necessarily overlay melting temperature versus hydrostatic stress for sapphire modestly above its HEL. We therefore plot shock-compression data
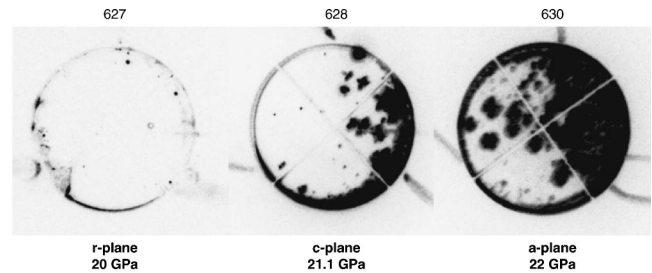

627   628   630

r-plane   c-plane   a-plane
20 GPa   21.1 GPa   22 GPa

FIG. 7. Shock-induced emission (negative) images for r-, c-, and a-plane sapphire for the lower stress range. Within this figure, emission intensity is quantitatively comparable. From left to right: r-plane at 20 GPa, c-plane at 21 GPa, a-plane at 22 GPa. 20 GPa is well beyond the r-plane HEL.

versus shock stress and hydrostatic compression data versus pressure. We believe the comparison is worthwhile but should not be expected to be perfect.

Temperatures for the homogeneous shock-compressed state of the base plate and window can be estimated based on the steady-shock conservation equations and a thermodynamic equation of state for the material. For our lower stress range (for computational purposes, taken as 22 GPa) the predicted final sapphire temperature is around 39 °C. Final baseplate temperatures (iron or stainless steel) should be less than 120 °C. For our higher stress range (taken as 45 GPa) the final sapphire temperature is predicted to be at 120 °C and the baseplate materials at less than 370 °C. There is a very serious disparity between these computed temperatures and T'.

Figure 6 shows four images of c-plane sapphire shocked to stresses from 11.5 to 21.8 GPa. This figure clearly demonstrates that for the c-plane case, the emission basically turns on between 13 and 22 GPa. Since the HEL of c-plane sapphire[8] is also reported to be within this stress range, the shock-induced emission appears to correlate with the onset of plastic deformation in sapphire, at least for the c-plane case.

We used fully oriented samples in an effort to correlate emission with slip on known crystal slip planes of sapphire. We found what can be at very best described as slight and admittedly somewhat subjective evidence for such a correlation. If such a correlation does exist for these three crystal orientations of sapphire, then it is much weaker than the effect previously demonstrated for X-cut α-quartz.[13,14]

Figure 7 shows a quantitative comparison of the shock-induced emission images at the low-end stress range 20–22 GPa. The c-plane and a-plane bright regions are heavily saturated due to the high effective gain conditions used for the detector for the low-end stresses. Clearly the r-plane sample emits less light than a- or c-plane. Figure 8 is, likewise, a quantitative comparison at the high-end stresses (40–47 GPa). It also shows that the r-plane again yields the least shock-induced emission of the three orientations. This clear dependence of the emission on sapphire crystal orientation and the apparent turning on of the emission at the sapphire HEL are two pieces of compelling evidence that the source of the emission is indeed the sapphire, and not the metal coating, glue joint, or baseplate that backs the sapphire.
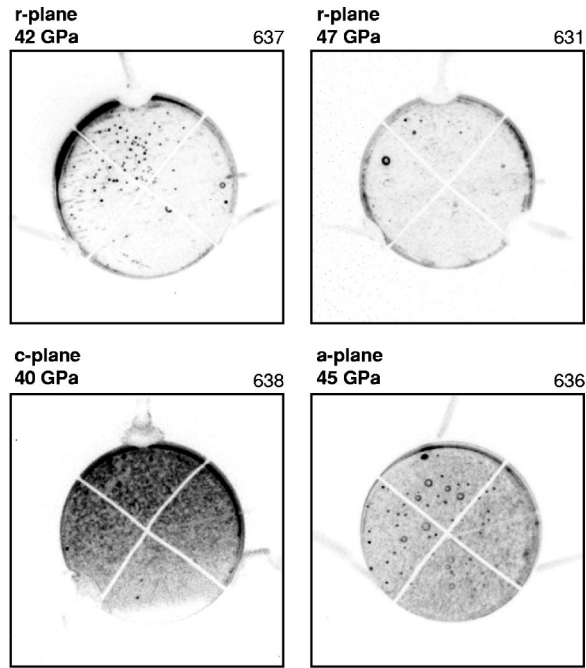
FIG. 8. Shock-induced emission (negative) images for r-, c-, and a-plane sapphire for the higher stress range. Within this figure, emission intensity is quantitatively comparable. Clockwise, starting from upper left: r-plane at 42 GPa, r-plane at 47 GPa, a-plane at 45 GPa, c-plane at 40 GPa.

IV. DISCUSSION

The heterogeneous nature of the shock-induced emission suggests shear banding as a plausible source of the emission. As our interpretation of the results invokes shear-banding theory,[28,29] a brief summary of this effect will be given here. A simple case example is illustrated in Fig. 9. Initially, material is undergoing plastic deformation at a constant (throughout space) shear-strain rate. This type of plastic shear deformation is unstable in materials which thermally soften. Shear flow stress is lower in regions of higher temperature. Reduced flow stress tends to funnel the global shear displacement into these warmer regions, causing a locally enhanced shear strain rate. Enhanced shear strain rate leads to increased frictional generation of heat, which further heats and softens the already hot area which again leads to yet higher local shear strain rates. This effect gives rise to a tendency for a homogeneously shearing, homogeneously heating body to evolve into a heterogeneous structure with a very narrow region of violent shear and heat generation adjacent to regions of rigid-body motion with no heat generation. This narrow region of intense localized shear flow is the shear band. We do not discount the possibility that material within the shear band could be heated beyond the melting point (the ultimate thermal softening!).

TEM studies of several crystal orientations of sapphire shock compressed and recovered from stresses up to 24 GPa indicate that twinning on the c-plane {0001} is the dominant deformation structure remaining in the recovered material, and also that these structures were minimal for the shocked c-plane sapphire.[30,31] It is easy to rationalize why deforma-
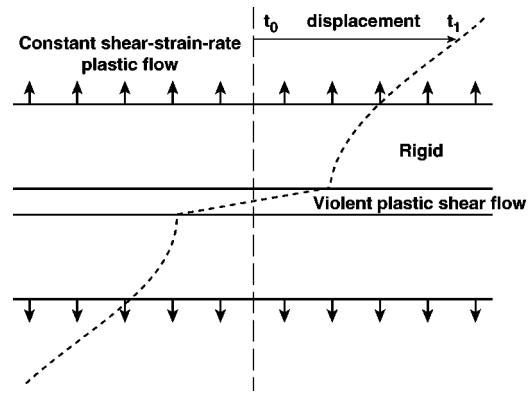

FIG. 9. Shear banding. The roughly micrometer-thick (Ref. 28) shear band and its associated rigid-body-motion region. This shear band/rigid structure grows at the expense of the constant shear-strain-rate plastic flow region.

tion on {0001} would be minimal in the case of c-plane samples since a longitudinal wave propagated exactly down the c-plane normal puts zero shear stress on {0001}. The a-plane orientation holds {0001} at 90° to longitudinal wave propagation down the a-plane normal. In this latter case the magnitude (see Appendix D) of the shear stress on {0001} is nonzero, but still small relative to the shock stress (5%, the magnitude of the ratio of the elastic constants c_{14}/c_{11}).[20] On the other hand, the r-plane orientation holds {0001} at 57.6° relative to the direction of shock propagation so that the magnitude of the shear stress on {0001} will be much larger (approximately 35% of the shock stress) than for the other two orientations.

The r-plane orientation shows reduced shock-induced emission. Hyun, Sharma, and Gupta showed that it has another interesting property: Its HEL is nearly a factor of 2 smaller than that of the a- and c-plane orientations (about 8.0–8.5 GPa for r-plane).[32]

As discussed above, deformation on {0001} is a conspicuous feature in shock-recovered sapphire samples. It is not clear whether this deformation occurred during the one-dimensional (1D) loading or complicated unloading process. If we assume this deformation was due to loading process then it is a plausible mechanism for the low HEL of r-plane sapphire, since the shear stress magnitude on {0001} is significantly greater for r-plane than for the other two orientations. Furthermore, if the shock-induced emission is in fact thermal incandescence, the reduced flow stress of r-plane (as manifested by the reduced HEL) shows that the viscous dissipation (the frictional heat source term in the energy equation) is reduced. All else being equal, this would imply reduced deformation zone temperatures and hence less thermal emission.

But even if the emission is not thermal incandescence, if the r-plane material endures the most deformation on {0001} and it always shows the least emission of the three orientations it seems reasonable to conclude that the prominent optical emission of a- and c-plane samples is not generated by twinning and slip on {0001}.

We have presented evidence that the observed shock-induced emission is associated with the inelastic deformation

of sapphire. Is this shock-induced emission thermal incandescence, or is it some nonthermal form of mechanoluminescence? We still do not know the answer to this. We lay out both cases for the reader to consider.

The case for nonthermal mechanoluminescence: Figure 5 shows that the melting temperature of sapphire increases with increasing hydrostatic pressure. The melting temperature is a natural place to pin the temperature of a shear band as will be explained momentarily. Yet Kondo's and our fitted temperatures of this emission seem to support an emission temperature which is independent of stress. Why does the measured emission temperature not increase with increasing shock stress in a similar fashion to the expected melt line behavior? Kondo also came to the conclusion that sapphire emission was some nonthermal form of mechanoluminescence. However, his conclusion was based on the emission appearing to increase as the sapphire started to unload. It is distinctly possible that the emission from unloading sapphire is due to an entirely different mechanism from the emission generated by the loading process.

The case for thermal incandescence: Referring again to Fig. 5: The pressure dependence of the melting temperature has not been experimentally determined beyond 26 GPa. The behavior of the melt line above this stress is supported entirely by simulation. There are disturbing inconsistencies between the simulation and the experimental data in their range of mutual overlap. The experimental data below about 8 GPa seem to agree with the Clausius-Clapeyron result. The simulation data clearly do not. There appears to be a change in slope of the experimental data at around 8 GPa which is not reproduced in the simulation and the experimental data above 8 GPa support a more gentle increase in melting temperature with pressure than does the simulation.

The emission-inferred temperatures are not right on the expected melt temperatures but they are not drastically off either. The emission temperatures are about 50% higher than the expected melt temperatures. The fit temperatures depend heavily on the gray-body assumption (that the spectral emissivity is wavelength independent). The gray-body assumption is purely expedient.

Why should thermal incandescence be expected to track the melt line? Most materials soften as the melting temperature is approached. If there is a discontinuous decrease in flow stress upon melting, then the viscous dissipation (the source term for the heat diffusion equation in shear banding) will basically turn off at melting. With the source off, the shear band temperature will decrease. Decreasing temperature favors resolidification. If the material starts to resolidify, the flow stress will abruptly increase and the source will turn back on, driving the temperature up again. It is a natural thermostat that tends to keep the shear band temperature near the melting temperature.

As a final observation, we note the appearance of bright circular rings of emission in certain images at the upper stress range (for example, shot 636 of Fig. 8). The size of the largest of these rings is about 0.5 mm in radius. If we assume that the source that made the largest ring has been in operation the longest time (this exposure was made about 140 ns after first entry of the shock wave into the sapphire) we get a crude estimate that the radius of the circular projection is growing at about 3–4 km/s (elastic shear wave speeds in sapphire are around 6 km/s). As these structures are almost perfectly circular in projection, the source which produced them is very small compared to 1 mm. Because there is not an obvious size gradient with respect to position on the image, the sources can not be confined to a planar region such as the chromium coating on the sample's upstream surface so that the source of this emission seems to be distributed throughout the bulk of the sample. These interesting structures are almost certainly connected with spherically or cylindrically symmetric stress waves of some sort but we do not attempt further speculation at present.

V. CONCLUSION

There is an extensive body of pre-existing work concerning shock-induced emission from sapphire. Our work extends previous knowledge by studying this emission for shock waves propagated in three different crystal directions using fully oriented single-crystal samples, and by imaging this emission in conjunction with spectroscopy of this emission. The most important result of this paper is that the emission intensity is significantly reduced for the case of *r*-plane orientation relative to the other two orientations studied (*a*- and *c*-plane). Although the source of this emission is linked to plastic deformation, it is not the plastic deformation most commonly found in shock-recovered sapphire samples, namely basal slip and twinning (deformation on {0001}). This is because the *r*-plane orientation yields the least emission intensity, but available evidence suggests it should endure the most basal deformation of the three orientations studied in this work.

ACKNOWLEDGMENTS

APPENDIX A: COMPUTATION OF SHOCK STRESS

The shock stresses which we reported for our sapphire samples and target baseplate (summarized in Table I) were computed according to standard proceedures used in the field of shock compression in condensed matter, which we outline very briefly below. Good references for this subject are Refs. 2 and 33–35. For the reasons mentioned in the Experimental Procedure section, the stresses computed by this method for (nonelastic) sapphire in the 13–30-GPa range should be considered approximate.

This appendix is not meant to be exhaustive or complete regarding the general theory of impact-generated stress waves in solids. It does, however, lay out the basic ideas and algebra necessary to generate Table I. It is intended to be kept simple and informative for the layperson seeking a very basic understanding of how the shock stress values of Table I were computed.

We begin by considering a steady planar shock wave propagating through a fluid. We use the example of a fluid for conceptual simplicity, but the resulting expressions are also applicable to shock compression of solids, provided that the stress variable is correctly interpreted.

The case of the steady planar shock wave is readily analyzed by considering a reference frame which travels at the same constant velocity as the shock front. In this reference frame, the steady shock wave is a time-independent structure with material flowing into the front region at constant velocity and exiting the front at a constant, but reduced velocity.

The continuity (conservation of mass), momentum, and energy equations of fluid dynamics in their one-dimensional steady-flow form may be applied directly to the steady shockwave flow pattern. The continuity and momentum equations are (respectively)

$$\rho_1 u_1 = \rho_0 u_0, \tag{A1}$$

$$p_1 + \rho_1 u_1^2 = p_0 + \rho_0 u_0^2. \tag{A2}$$

p_0, ρ_0, and u_0 are the fluid pressure, mass density, and flow velocity ahead of the shock front. The subscript "1" applies to the same quantities behind the front (note: the energy equation is not usually needed when computing shock stress by the method which we outline here).

A particularly useful expression is obtained by transforming the continuity and momentum relations into a reference frame at rest with respect to the material ahead of the front ($p = p_1 - p_0, u_1 = U_s, u_2 = U_s - U_p$) and then appropriately combining them to eliminate ρ_1

$$p = \rho_0 U_s U_p. \tag{A3}$$

Here, U_s is the shock front propagation velocity relative to the material ahead of the front, and U_p is the particle velocity of the shock-compressed material behind the front with respect to the material ahead of the front. The direction of U_p is to flow towards the front. In fluids, p is the increase in fluid pressure behind the shock front with respect to the pressure ahead of the shock front.

We used the example of a shock wave in a fluid because of familiarity that much of the readership probably has with the elements of fluid dynamics. It turns out that the concepts of conservation of mass, momentum, and energy are equally applicable to shock waves in solids and Eq. (A3) is still applicable, provided that p is given a slightly different interpretation. p must now be reinterpreted as the increase in normal stress on a plane which is co-planar with the shock front. p as reinterpreted for solids is refered to as the "shock stress" throughout this paper.

Using Eq. (A3) we can construct the (very useful) loading curve of p versus U_p for a given material. To do so, we must know the material's initial state mass density, and also know the mathematical relationship between U_s and U_p for the material. This latter functional relationship is frequently refered to as a "Hugoniot." There is a unique Hugoniot for each unique initial state of each material, and each Hugoniot is usually determined through numerous shock compression experiments on the same material starting from the same initial state. The most widely known and used Hugoniots have the RTP (room temperature and pressure) state as the initial state and unless otherwise stated the term "Hugoniot" will mean the Hugoniot with the RTP initial state. It is found empirically that the simple linear form

$$U_s = c + s U_p \tag{A4}$$

is adequate over a large range of shock stress for many materials, including the impactor and baseplate materials used in this work.

Under conditions which are met by tilt-free, normal incidence, high velocity impacts in most materials, the impact process launches two counterpropagating, steady shock waves: one in the impactor and one in the baseplate. There are two boundary conditions for this case: (i) net shock stress is continuous, and (ii) net particle velocity is also continous across the (sample baseplate) junction after impact. Arithmetically speaking, these two conditions are expressed as follows:

$$p_A = p_B, \tag{A5}$$

$$U_f - U_{pA} = U_{pB}. \tag{A6}$$

Here the subscripts A and B denote the impactor and baseplate, respectively. U_f is the velocity of the impactor (the "flyer") before impact. The negative sign in front of U_{pA} is because the shock wave in the impactor propagates in the opposite direction to the motion of the flyer and the shock wave in the baseplate.

The above impact boundary conditions have a very nice visual representation in the form of a p versus U_p plot. In such a plot, the baseplate is represented by its p vs U_p curve centered on $p = 0$, $U_p = 0$. The impactor is represented by its p vs U_p curve reflected about the plane $U_p = 0$ (because the impactor wave counterpropagates relative to the baseplate wave) and also translated from $p = 0$, $U_p = 0$ to $p = 0$, $U_p = U_f$ (because prior to impact, the impactor is in the initial state $p = 0$, $U_p = U_f$). The reader can convince his/herself that the two boundary conditions above are satisfied at the intersection of the baseplate and impactor curves and there-
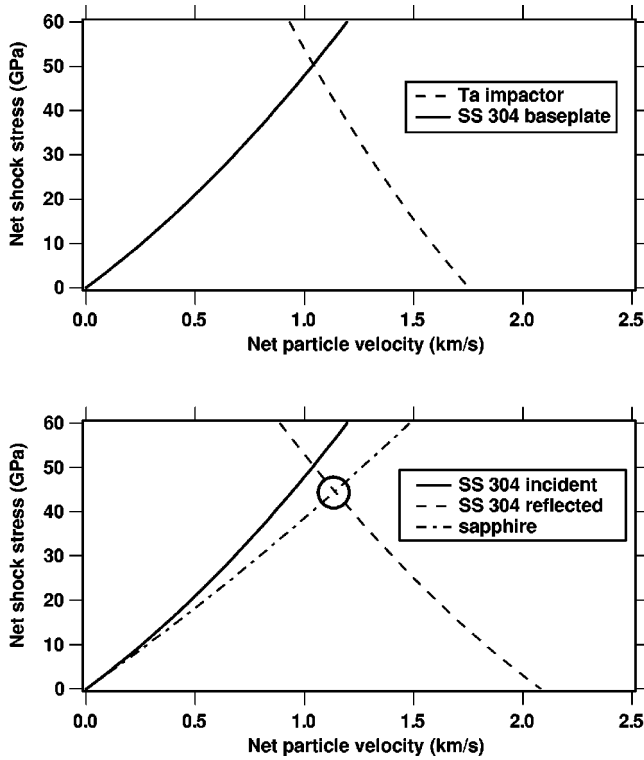
FIG. 10. The data of shot 635, $U_f = 1.754$ km/s. Top: The p vs U_p plot for the tantalum impactor on the 304 stainless-steel baseplate. The crossing point of the two curves gives the shock stress generated in the baseplate. Bottom: The p vs U_p plot for the resulting shock wave incident from the SS 304 baseplate, transmitted into the sapphire sample. The crossing point of the SS 304 reflected and sapphire curves (circled in figure) gives the computed shock stress in the sapphire sample. The tantalum Hugoniot is from Ref. 18. The SS 304 and sapphire Hugoniots are from Ref. 17.

fore p and U_p of the loaded baseplate is simply given by this intersection on the p versus U_p plot. This is illustrated in Fig. 10.

We have just outlined how to determine the shock stress generated in the baseplate due to the impactor. How does this shockwave from the baseplate transmit into the sapphire sample? This latter case is more like familiar optics phenomena; there are now three waves to consider: (i) a shock-wave incident on a stationary baseplate sample junction; (ii) a shock wave transmitted into the sample; (iii) a wave reflected by the junction back into the baseplate. This reflected wave can be either a shock or rarefaction wave depending on whether the shock impedance (i.e., the product $\rho_0 U_s$) of the sample is greater than, or less than that of the baseplate, respectively.

As with the direct impact case, the appropriate boundary conditions are continuity of the net shock stress and net particle velocity across the junction. This can be written as

$$p_{Bi} + p_{Br} = p_C, \tag{A7}$$

$$U_{pBi} - U_{pBr} = U_{pC}. \tag{A8}$$

B and C are the baseplate and sample materials, respectively. i and r indicate the incident and reflected waves, respec-

tively. The sign convention here is that p and U_p are positive quantities for compressive waves, regardless of direction of wave propagation. As with Eq. (A6), the negative sign in front of U_{pBr} in Eq. (A8) indicates that the reflected wave propagates in the opposite direction to the transmitted wave.

Once again it is useful to construct a p vs U_p plot. Both the incident wave from the baseplate and the transmitted wave into the sample start at $p=0$, $U_p=0$. The loading (or unloading!) curve for the reflected wave in the baseplate contacts the incident wave p versus U_p plot loading curve at the incident wave stress $p=p_{Bi}$. It faces in the opposite direction to the other two curves (i.e., it counterpropagates). Because this reflected wave loading curve (1) starts from a non-RTP initial state (2) may be a rarefaction wave (unloading) rather than a shock wave, it must be either computed or deduced by approximate methods. A very common approximation is to use the reflection of the incident wave loading curve about the plane $U_p = U_{pBi}$. It is found that this approximation is reasonable for junctions of relatively incompressible materials which are loaded to not too extreme stresses: conditions which apply to the experiments of this work. The transmitted wave state (p_C, U_{pC}) is given by the intersection of the transmitted wave loading curve and the reflected wave loading curve. This is also illustrated in Fig. 10.

The equivalent algebraic result for the impactor-baseplate process is given by the following quadratic equation for U_{pB} in which all the other quantities are known:

$$\rho_{0A}[c_A + s_A(U_f - U_{pB})](U_f - U_{pB})$$
$$= \rho_{0B}(c_B + s_B U_{pB})U_{pB}. \tag{A9}$$

When Eq. (A9) is put into standard quadratic form and solved, the solution with the negative sign in front of the square root is the physical solution for U_{pB}. The shock stress generated in the baseplate is then just a straightforward application of Eq. (A3) with the Hugoniot for the baseplate substituting U_{sB}:

$$p_B = \rho_{0B}(c_B + s_B U_{pB})U_{pB}. \tag{A10}$$

The algebraic description of the baseplate sample problem (incorporating the reflected wave approximation) results in this quadratic equation for U_{pC}:

$$\rho_{0B}[c_B + s_B(2U_{pBi} - U_{pC})](2U_{pBi} - U_{pC})$$
$$= \rho_{0C}(c_C + s_C U_{pC})U_{pC}. \tag{A11}$$

Since U_{pBi} is known (it is U_{pB} from the impactor-baseplate solution) Eq. (A11) is readily solved for U_{pC}. Again, the "negative sign" solution is the physical solution and p_c (i.e., the sample shock stress) is computed in same fashion as Eq. (A10).

In summary, what is required to compute shock stress in the sample is to know the impactor velocity, and the RTP mass density and Hugoniot for each of the impactor, baseplate, and target. p_B will give the baseplate shock stress ("in-

cident stress'' column of Table I) and p_C will give the reported shock stress in the sapphire sample (''nominal stress'' column of Table I).

APPENDIX B: SAPPHIRE UNIT-CELL CONVENTIONS

In this paper we follow the Bravis-Miller indexing convention of the x-ray (also known as ''structural'') hexagonal cell. For the other common (i.e., morphological hexagonal cell) convention, the r-plane indexing is $\{10\bar{1}1\}$. c- and a-plane indices are the same in both conventions. The reader is cautioned that workers in the field of sapphire do not always make it obvious which convention they are using. The reader is further cautioned that there is another family of sapphire crystal planes denoted by upper-case ''R'': that these planes are not equivalent to the lower-case ''r'' planes of interest in this publication. It is a very unfortunate coincidence that the indices of the R-planes in the morphological cell (i.e., $\{1\bar{1}02\}$) are identical to the indices of the r-planes in the x-ray cell. References 36, 37, and 20 may be of help to the reader.

APPENDIX C: COMMENTS ON RADIOMETRY

Spectral emissivity is the ratio of the spectral radiant emittance of a real thermal body to that of an ideal blackbody at the same temperature and wavelength. Recall that spectral radiant emittance has units of power radiated per unit radiator surface area per unit wavelength. The fitted quantity we define as ''apparent emissivity'' is actually the ratio of the spectral irradiance at our spectrograph's optical fiber entrance (total power per unit area incident on the fiber core entrance surface per unit wavelength, which includes both propagating and nonpropagating modes of the fiber) to the spectral radiant emittance of a blackbody at the fitted (i.e., ''apparent'') temperature and same wavelength. Because spectral irradiance has the same units as spectral radiant emittance, our apparent emissivity has the same units as the genuine spectral emissivity (dimensionless). In the context of fitting spectra, the gray-body approximation is that our apparent emissivity is taken to be a constant, independent of wavelength.

APPENDIX D: SAPPHIRE BASAL PLANE DEFORMATION

For the purpose of estimating shock stresses required to cause twinning and slip on $\{0001\}$ we compute the magnitude of the shear stress resolved on $\{0001\}$ without attention to the direction of resolution in this plane. The symmetry of sapphire confers a certain amount of directional independence to deformation on $\{0001\}$. For example, the threefold symmetry axis normal to $\{0001\}$ insures that there is always at least one deformation system in the basal plane on which the magnitude of the directionally resolved shear stress is more than half of the magnitude of the total shear stress on the basal plane.

[1] There are occasional examples of rarefaction shock waves caused by phase transitions or found in materials with unusual mechanical properties, but they are not relevant to the present discussion.

[2] Ya. B. Zel'dovich and Yu. P. Raizer, *Physics of Shock Waves and High-Temperature Hydrodynamic Phenomena*, edited by W. D. Hayes and R. F. Probstein (Academic Press, New York, 1966), p. 685.

[3] J. L. Wise and L.C. Chhabildas, in *Shock Waves in Condensed Matter-1985, Proceedings of the Fourth APS Topical Conference on Shock Waves in Condensed Matter, Spokane, WA, July 22-25, 1985*, edited by Y. M. Gupta (Plenum, New York, 1986), p. 441.

[4] F. Schmid, C. P. Khattak, and D. M. Felt, Laser Focus World **32**, 167 (1996).

[5] L.M. Barker and R.E. Hollenbach, J. Appl. Phys. **41**, 4208 (1970).

[6] P.A. Urtiew, J. Appl. Phys. **45**, 3490 (1974).

[7] R.G. McQueen and D.G. Isaak, J. Geophys. Res. **95**, 21 753 (1990).

[8] R. L. Webb, M. S. thesis, Washington State University, 1990.

[9] K. Kondo, in *Joint International Association for Research and Advancement of High Pressure Science and Technology and American Physical Society Topical Group on Shock Compression of Condensed Matter Conference, Colorado Springs, CO*, (American Institute of Physics, New York, 1994), p. 1555.

[10] David A. Young (private communication).

[11] Ya. B. Zel'dovich and Yu. P. Raizer, *Physics of Shock Waves and High-Temperature Hydrodynamic Phenomena* (Ref. 2), p. 46.

[12] C. S. Kwiatkowski and Y. M. Gupta, in *Shock Compression in Condensed Matter: Conference in Snowbird, Utah, June 1999*, edited by M. D. Furnish, L. C. Chhabildas, and R. S. Hixson, (American Institute of Physics, Melville, 2000), p. 641.

[13] W.P. Brooks, J. Appl. Phys. **36**, 2788 (1965).

[14] P. J. Brannon, R. W. Morris, C. H. Konrad, and J. R. Asay, in *Shock Waves in Condensed Matter—1983*, edited by J. R. Asay, R. A. Graham, and G. K. Straub (North-Holland, Amsterdam, 1984), p. 303.

[15] H. Winchell, Bull. Geol. Soc. Am. **57**, 295 (1946).

[16] A.H. Jones, W.M. Isbell, and C.J. Maiden, J. Appl. Phys. **37**, 3493 (1966).

[17] LASL Shock Hugoniot Data, edited by Stanley P. Marsh (University of California Press, Berkeley, 1980).

[18] N.C. Holmes, J.A. Moriarty, G.R. Gathers, and W.J. Nellis, J. Appl. Phys. **66**, 2962 (1989).

[19] R.A. Graham and W.P. Brooks, J. Phys. Chem. Solids **32**, 2311 (1971).

[20] J.M. Winey, Y.M. Gupta, and D.E. Hare, J. Appl. Phys. **90**, 3109 (2001).

[21] W. J. Smith, *Modern Optical Engineering: The Design of Optical Systems*, 2nd ed. (McGraw-Hill, New York, 1990), p. 217.

[22] Charles Kittel and Herbert Kroemer, *Thermal Physics*, 2nd ed. (W. H. Freeman and Co., New York, 1980), p. 94.

[23] Guoyin Shen and Peter Lazor, J. Geophys. Res. **100**, 17 699 (1995).

[24] Zhongwu Wang, Huahai Mao, and S.K. Saxena, J. Alloys Compd. **299**, 287 (2000).

[25] Charles Kittel and Herbert Kroemer, *Thermal Physics* (Ref. 22), p. 281.

[26] P. Tyrolerova and W.-K. Lu, J. Am. Ceram. Soc. **52**, 77 (1969).

[27] *CRC Handbook of Chemistry and Physics*, editor-in-chief: David R. Lide, 78th ed. (CRC Press, New York, 1997), p. 6-116.

[28] D.E. Grady and M.E. Kipp, J. Mech. Phys. Solids **35**, 95 (1987).

[29] D.E. Grady, J. Mech. Phys. Solids **40**, 1197 (1992).

[30] Y. Wang and D.E. Mikkola, Mater. Sci. Eng., A **148**, 25 (1991).

[31] S.J. Chen and D.G. Howitt, Philos. Mag. A **78**, 765 (1998).

[32] J. Hyun, S.M. Sharma, and Y.M. Gupta, J. Appl. Phys. **84**, 1947 (1998). The *r*-plane HEL is listed as 6.5 GPa in this reference, but in a recent private communication, Y. M. Gupta informed us that the slightly higher stress 8.0–8.5 is more accurate.

[33] M. H. Rice, R. G. McQueen, and J. M. Walsh, in *Solid State Physics: Advances in Research and Applications*, edited by Frederick Seitz and David Turnbull (Academic Press, New York, 1958), p. 1.

[34] M. B. Boslough and J. R. Asay, in *High Pressure Shock Compression of Solids*, edited by James R. Asay and Mohsen Shahinpoor (Springer-Verlag, New York, 1992), p. 7.

[35] H. Kolsky, *Stress Waves in Solids* (Dover, New York, 1963).

[36] C. Palache, H. Berman, and C. Frondel, *Dana's System of Mineralogy*, 7th ed.(Wiley and Sons, New York, 1944), p. 520.

[37] M.L. Kronberg, Acta Metall. **5**, 507 (1957). Especially see Appendix C of this reference.